Inner Front Pole Cover Erosion in the 12.5 kW HERMeS Hall Thruster Over a Range of Operating Conditions

IEPC-2017-409

Presented at 35th International Electric Propulsion Conference
Atlanta, Georgia
October 8–12, 2017

James E. Polk* and Robert Lobbia†
Jet Propulsion Laboratory, California Institute of Technology, Pasadena, CA 91109, USA

Arthur Barriault‡
University of Colorado Boulder, Boulder, CO 80309

Pablo Guerrero §
California Institute of Technology, 1200 E. California Blvd., Pasadena, CA 91125

Ioannis Mikellides¶ and Alejandro Lopez Ortega‖
Jet Propulsion Laboratory, California Institute of Technology, Pasadena, CA 91109, USA

Erosion characteristics on the cover of the inner front pole in a 12.5 kW Hall thruster were measured over a wide range of operating conditions in tests of 6 to 14 hours duration using an accelerated test method and a very sensitive radioactive tracer-based erosion diagnostic. The operating points included the nominal 300 - 600 V conditions on a constant 20.8 A throttle curve, but included additional conditions at other currents spanning the throttling envelope and measurements at varying magnetic field strength, facility pressure, and discharge voltage oscillation amplitude. The results show that the 300 V condition produces the highest wear rates on the 20.8 A throttle curve, but that rates actually increase with decreasing current. The wear rate was insensitive to discharge voltage ripple, but increased monotonically with magnetic field strength, particularly near the inner radius of the pole cover. The inner region was also sensitive to facility pressure, showing lower rates at a higher pressure level. Separate experiments in which the energy distributions of ions generated by the hollow cathode were measured suggest that the cathode plume may be a source of energetic ions responsible for some of the erosion trends, in addition to ions originating in the thruster plume. The Hall thruster simulation code Hall2De is able to reproduce the erosion characteristics observed at 600 V, 20.8 A, but cannot currently match the rates measured at lower voltages and currents.

*Principal Engineer, Propulsion and Materials Engineering Section, james.e.polk@jpl.nasa.gov
†Staff Engineer, Electric Propulsion Group, robert.b.lobbia@jpl.nasa.gov
‡Graduate student, arthurbarriault@gmail.com
§Graduate student, GALCIT Aerospace Department, pguerrer@caltech.edu
¶Principal Engineer, Electric Propulsion Group, ioannis.g.mikellides@jpl.nasa.gov
‖Senior Engineer, Electric Propulsion Group, alejandro.lopez.ortega@jpl.nasa.gov¿
©2017. All rights reserved.

I. Introduction

Solar electric propulsion (SEP) is a key technology for future human and robotic exploration missions and is now an integral part of NASA's vision for expanding human presence beyond low earth orbit. Since 2012 the NASA Glenn Research Center (GRC) and the Jet Propulsion Laboratory (JPL) have worked jointly to mature Hall thruster technology for a 40-50 kW system.[1] This work has been supported primarily by the Space Technology Mission Directorate under the SEP Technology Demonstration Mission project with the goal of providing flight hardware for the first user of a high power electric propulsion system.[2,3] The Asteroid Robotic Redirect Mission (ARRM), an ambitious mission concept that would have been enabled by high power SEP, was the intended target application until it was cancelled early in 2017.[4] Work with the ARRM project helped shape the requirements for the system though, and a potential new user for a system similar to that envisioned for ARRM is the Power and Propulsion Element, a module providing propulsion for the proposed Deep Space Gateway. This vehicle, which would also include a crewed habitat, is being considered for operation in lunar orbit to help develop capabilities for future human Mars missions.[5]

The technology program has focused on the development of a thruster and power processing unit (PPU) for a 13.3 kW string. Three of these strings (plus a spare string) would form a 40 kW system. The Hall Effect Rocket with Magnetic Shielding (HERMeS), one product of the joint GRC-JPL development, incorporates a number of Hall thruster innovations developed over the last two decades.[6] Three technology development units (TDUs) like the one pictured in Fig. 1 were built for performance, environmental, and wear tests, as well as focused risk reduction tests. The HERMeS TDUs have demonstrated operation at discharge voltages ranging from 300 to 800 V and discharge currents from 6 to 31.2 A. This corresponds to power levels up to 12.5 kW, thrust levels as high as 680 mN, and specific impulses up to 3000 s.[7]

The Advanced Electric Propulsion System (AEPS), which is being developed by Aerojet Rocketdyne as prime and VACCO and ZIN Technologies as sub-contractors under a competitively-awarded contract, includes design and testing of engineering development units (EDUs) based on NASA's HERMeS thruster and PPU development and a xenon feed system. In a subsequent option phase a qualification string and four flight strings would be delivered.[8] The performance requirements for the AEPS are based on a subset of the throttling envelope with voltages ranging from 300 to 600 V and a fixed discharge current of 20.8 A. The xenon throughput requirement is 1770 kg per thruster, yielding a total throughput capability of over 5300 kg for the 40 kW system. The advanced system development is a coordinated activity with an integrated NASA/industry team. NASA is providing support to Aerojet Rocketdyne in several areas, particularly testing, risk reduction and life qualification activities.

Figure 1. The HERMeS 12.5 kW Hall thruster.

The target missions for the AEPS have very high throughput requirements, which is a significant design driver. One key technology is magnetic shielding, which involves a carefully engineered magnetic field topology and discharge chamber configuration that prevents bombardment of the discharge channel wall by high energy ions. The development of the magnetic shielding design approach was motivated by the observation that channel erosion essentially stopped in the qualification wear test of Aerojet Rocketdyne's XR-5 Hall thruster after 5600 hours.[9] The physics responsible for this were first identified in simulations of the XR-5 at JPL using the Hall thruster plasma simulation code Hall2De[10,11] and were validated in tests at JPL with a modified version of the laboratory model H6 thruster, designated the H6MS (for magnetic shielding).[12,13] Subsequent tests showed that magnetic shielding could be effective at high specific impulse[14,15] and joint testing with NASA GRC demonstrated that a high power Hall thruster could be modified to incorporate magnetic shielding.[16] HERMeS is the first thruster designed from the outset to incorporate magnetic shielding and a number of experiments and simulations have verified that discharge channel erosion, which

was previously the main life-limiting process in Hall thrusters, has been eliminated as a credible failure mode.[17,18]

However, the thruster is subject to other potential failure modes, and the one of greatest concern currently is erosion of the inner front pole. Erosion of this component appears to be a consequence of magnetic shielding, which moves the acceleration zone further downstream and produces potential gradients at the edge of the beam that result in greater divergence of high energy ions, although the rates of pole erosion are much lower than the rates of channel erosion in unshielded thrusters.[19] Pole erosion was first observed in a 150 hour wear test of the H6MS at 300 V (2000 s Isp) and 6 kW and was further characterized in a series of short duration wear tests, including a 100 hour test at 800 V (3000 s Isp) and 9kW.[14] A second 150 hour wear test at 300 V and 6 kW incorporated a sputter-resistant graphite pole cover instrumented with radial strips of molybdenum, which served as masks for the graphite cover and were themselves masked so the wear rate could be measured on them as well.[20] The masks provided uneroded reference surfaces that could be compared to the eroded surfaces using an optical profilometer. These measurements yielded graphite erosion rates of 25-71 μm/khr and molybdenum wear rates of 120-270 μm/khr. The erosion profile peaked at inner and outer edges of the face of the graphite cover.

A subsequent 1722 hour test of TDU-1 was conducted to characterize wear rates in the HERMeS thruster.[21] The test consisted of four segments with several different configurations, but in two of these segments (II and IV) the wear rates of graphite covers with molybdenum witness strips were measured for thruster operation at 600 V and 20.8 A. The duration of segment II was 246 hours and segment IV lasted 996 hours. The erosion profiles were similar to those observed on the H6MS pole cover, with rates on graphite that ranged from 10-45 μm/khr (segments II and IV) and rates on molybdenum of 100-600 μm/khr (based on measurements conducted at two times during segment II). A systematic variation in the erosion rates for both materials by up to a factor of two between various test segments was noted.

These tests provided critical initial data on wear rates; in particular, providing confidence that graphite pole covers of reasonable thickness could protect the pole underneath for the required thruster lifetimes. However, these tests were time-consuming and very expensive to perform. To get sufficient wear for reliable profilometer measurements at a single point, the thruster must be operated for on the order of $150 - 200$ hours, so it is not feasible to use this approach to obtain wear rate data over a large range of parameters.

The tests reported here used an accelerated testing method and a very sensitive erosion measurement technique to answer specific questions about the behavior of pole cover erosion with individual erosion tests of only 6–14 hours. Data over a larger range of operating parameters are required to help plan future wear tests, to identify and characterize key drivers of pole erosion, to guide model development and to help validate models. The specific objectives of these tests included:

- Characterize the pole erosion rates over a broad range of operating conditions
- Identify the worst case operating point for nominal HERMeS operating conditions
- Determine sensitivity to discharge voltage and current
- Determine sensitivity to other parameters such as magnetic field strength, magnitude of discharge voltage ripple, and facility background pressure

The Surface Layer Activation (SLA) technique employs a radioactive tracer in a thin layer near the surface of a component to measure erosion. As material is removed from the surface, the activity level drops. The activity before and after an erosion test is measured with a standard gamma ray spectroscopy system, and if the erosion is uniform over the activated spot, the change in activity can be related to the depth change with a calibration curve. The SLA technique is non-intrusive and can resolve sub-micron depth changes, so it is well-suited to applications in harsh environments with low erosion rates. In these tests the SLA diagnostic was used with a molybdenum pole cover. Molybdenum was chosen for several reasons. First, its sputter yield is higher than that of graphite so it accelerates the wear rate, yielding micron-scale depth changes in short duration tests. Second, SLA using molybdenum is a mature diagnostic technique. The activation technique used to produce the radioactive tracer was developed for industrial applications of SLA[22] and it was used in measurements of ion engine keeper erosion at JPL.[23,24] These tests demonstrated the required sensitivity and were validated by comparison to wear rates from the 8200 hour wear test of the NSTAR

ion thruster. Finally, the SLA measurements could be compared to erosion measurements on molybdenum witness samples from longer duration tests like those described above.

Sputter yields measured as a function of bombarding ion energy for xenon on molybdenum and graphite are shown in the two plots in Fig. 2, which are reproduced from a review by Yim[25] (see Yim's paper for the references to sputter yield measurements cited in the plots). The curve fits to the data are based on Eckstein's semi-empirical model with maximum likelihood fit coefficients obtained in Yim's detailed analysis.[25] The bands represent the 50% likelihood limits for the fit parameters estimated using a Bayesian approach with a nested sampling routine based on a Markov chain Monte Carlo method. Sputter yield data are sparse at energies below 50 eV and there is considerable scatter at higher energies, which is reflected in the width of the 50% likelihood bands. These fit curves are shown together in terms of atoms removed per bombarding

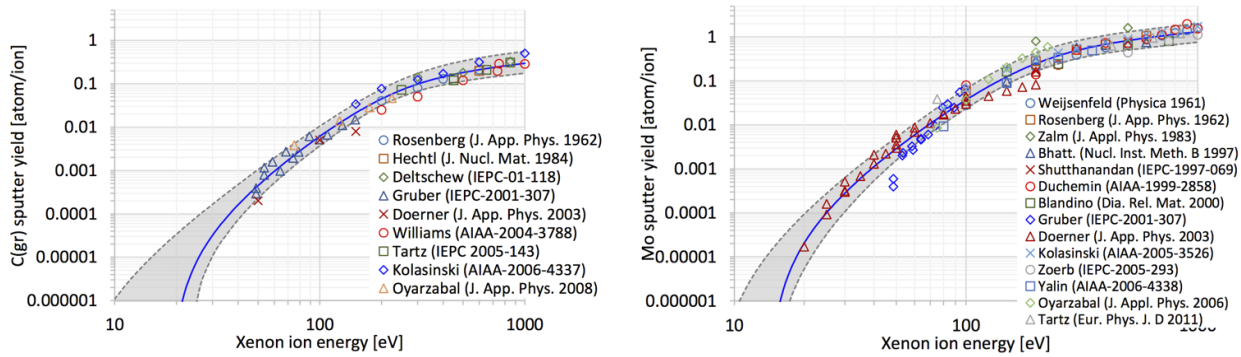

Figure 2. Sputter yield data for xenon incident on carbon (left) and molybdenum (right).[25]

ion and also as the volume of material removed per 6.242×10^{18} ions in the left plot in Fig. 3. For singly charged ions this corresponds to mm^3 removed per Coulomb of charge. The ratio of molybdenum to graphite yields is plotted on the right side of Fig. 3. For the ratios at non-normal incidence the Wei semi-empirical formula with fit coefficients recommended by Yim is used.[25] For most of range of interest (up to several hundred eV) the wear rate acceleration factor associated with using molybdennum instead of graphite for normal incidence is 8-10. Higher incidence angles reduce the acceleration factor because the graphite sputter yield increases more with angle compared to molybdenum. For energies less than about 35-40 eV, the ratio increases rapidly because the yield models predict a more rapid drop in yield near a somewhat higher threshold energy for graphite sputtering. There is considerable uncertainty in both yield models, so it would

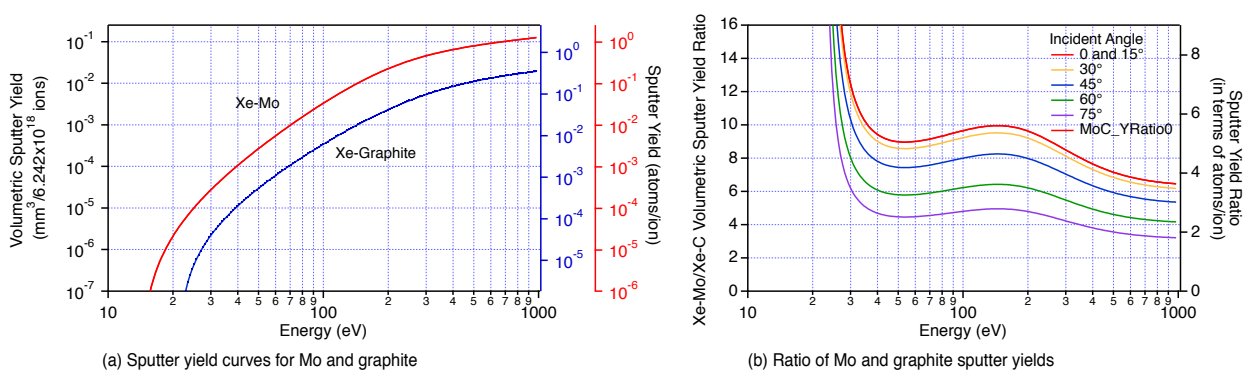

Figure 3. Curve fits to the sputter yield data (left) and the ratio of yields for molybdenum compared to graphite (right).

be difficult to accurately scale the results of the accelerated tests to wear rates expected for graphite pole covers. The primary value of these accelerated tests is in defining relative erosion rates between operating points, identifying the primary drivers of pole erosion, and providing additional data to validate erosion models, which can be run with molybdenum sputter yields for direct comparison to these data.

In this paper we first discuss the SLA technique in more detail and describe the erosion measurements. Some of the data suggested that the cathode plume may also be source of high energy ions, in addition to the thruster plume, so a separate experiment designed to determine the high energy ion content of the hollow cathode plume is described. After presenting the erosion data, we discuss variability in the measured rates, the role of the cathode plasma, and how these experiments contribute to the current understanding of pole erosion.

II. The Surface Layer Activation Technique

The Surface Layer Activation technique was originally developed by the Nuclear Physics Division at the AERE Harwell Laboratory[26–29] and has been used in a number of different applications, including measuring component wear in internal combustion engines[27] and turbines,[30] corrosion in chemical plants,[31] unipolar arcing damage in tokomaks[32] and wear in prosthetic hip joints.[29] It has also been employed to measure the erosion rates of tungsten cathodes, copper anodes and boron nitride backplates in magnetoplasmadynamic (MPD) thrusters[33–35] and, as noted above, molybdenum keeper electrodes in ion thrusters.[23,24]

The SLA technique relies on three processes: the production of the radioactive tracer in the component surface layer, measurement of the initial activity level and the activity level before and after an individual erosion test, and calibration of the activity level with depth.

A. Component Labeling with the Radioactive Tracer

There are several techniques for producing a radioactive tracer in a thin layer near the surface of a component to be tested.[22] The method used here involves bombarding the component with a high energy particle beam produced in a commercial cyclotron or van de Graaff accelerator, which transmutes a tiny fraction of the target material atoms to a gamma-emitting radionuclide. For our components we used an 11 MeV proton beam to produce the radioisotope ^{95m}Tc, which is formed when an energetic proton interacts with a molybdenum nucleus and ejects one neutron in the reaction ^{95}Mo(p,n)^{95m}Tc. This isotope is a good choice for SLA because it is a high yield reaction (defined in terms of the amount of activity produced per Coulomb of proton charge on the target) and it has a half life of 62 days, so experiments can be conducted over several months before the gamma signal becomes too low to use. A second high yield reaction generates ^{96}Tc, which has a number of gamma lines that interfere with those from ^{95m}Tc. Fortunately the half life of ^{96}Tc is only 4.3 days, so if the parts are allowed to "cool off" for two months after activation, the ^{96}Tc decays to a negligible level compared to the ^{95m}Tc isotope.

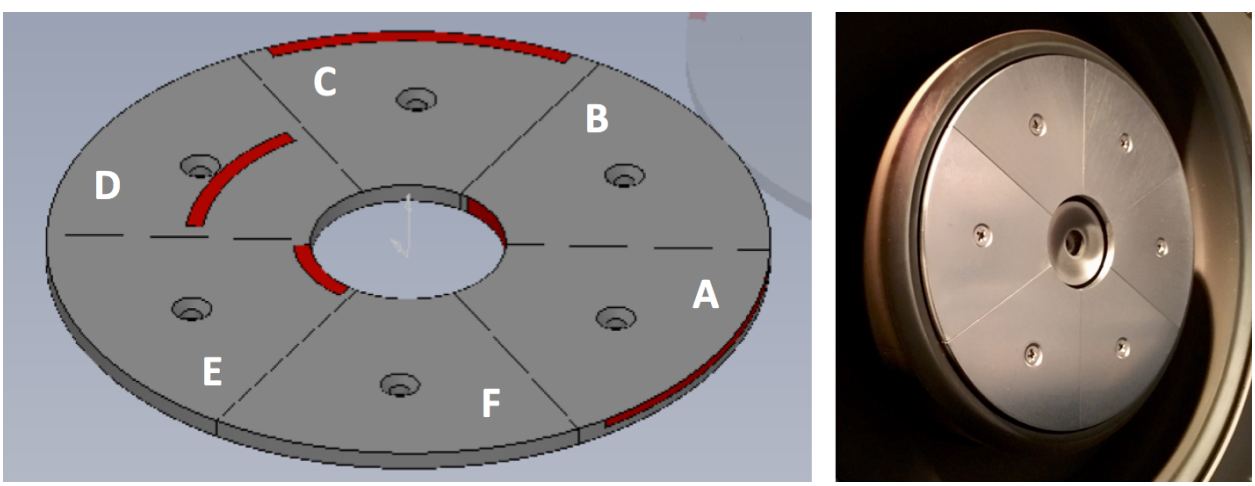

Figure 4. Schematic showing the activated regions on individual pole segments (left) and photo of the activated pole cover mounted on the thruster (right).

Like any process governed by binary collisions, the nuclear reaction rate can be described by an energy dependent cross section. Accelerators produce beams that have very little spread in energy, so the only

significant energy variation occurs along the beam path in the material as the particles lose energy in collisions with target atom electrons and nuclei. The total range is determined by the stopping power of the material, which depends on the cross sections for energy transfer to electrons and nuclei . For 11 MeV protons normally incident on molybdenum, the energy drops to about 4 MeV at a depth of 235 microns. This is the threshold energy for the ^{95}Mo(p,n)^{95m}Tc reaction, so no more tracer material is produced below that depth. To increase the sensitivity of the technique, the depth of the activated layer can be compressed by a factor of $\cos(\theta)$ by activating with a beam at an incident angle of θ with respect to the target surface normal.

Two pole covers composed of six segments machined from high purity molybdenum, as shown in Fig. 4, were activated for this experiment. The left hand image is a schematic showing the activated spots. We expect significant variation in wear rates radially because of axisymmetry in the thruster geometry. The activated regions are therefore relatively thin in the radial direction to give good spatial resolution, but the tracer material was spread over an arc in the azimuthal direction to provide high signal strength at proton doses that would not cause radiation damage in the target. Custom tantalum masks were used to shield regions on each segment that were not to be activated. The targets were irradiated with a beam incidence angle of 60° to compress the activated layer by a factor of two.

Segment A of both sets was activated in a thin strip on the downstream half of the outer diameter. The upstream half of the pole cover is shadowed from the plasma by the inner ceramic wall of the discharge chamber, so we did not expect the erosion rate there to be the same as on the downstream half. Segment B was activated on the inner diameter face. In this case the activated spot extended all the way upstream because this entire face is exposed. A thin strip several mm wide was activated along the outer downstream face of Segment C. Segment D was activated near the mid-radius, although the fastener hole had to be avoided. A similar strip on the inner radius of the downstream face of Segment E was bombarded. Segment F was not activated and served as a blank that was periodically checked to verify that no radioactive material was being transferred from one segment to another. The parts were activated by ANS Technologies using a tandem van de Graaff accelerator in the Laboratoire René-J.-A.-Lévesque at the University of Montreal. After the cooling off period the activity level of the individual spots ranged from 2 to 10 μCi. The photograph on the right side of Fig. 4 shows one of the activated sets mounted on the thruster.

B. Gamma Spectroscopy and Analysis

The activity level is determined using a gamma ray spectroscopy system which consists of a semiconductor or scintillator detector that produces voltage pulses with an amplitude proportional to the absorbed gamma ray energy and a pulse height analysis system that bins pulses according to their amplitude to produce an energy spectrum like those shown in Fig. 5. The count rate is the number of gamma rays detected per second in a given channel, which corresponds to a discrete energy range. The spectrum shown on the left was obtained from one of the activated samples using a 7.5 cm diameter by 7.5 cm long NaI scintillator crystal and photomultiplier tube (PMT) from Scintitech. When a gamma ray is absorbed in the NaI crystal it produces optical photons which are converted by the PMT and associated pre-amplifier into a voltage pulse. These pulses were collected and analyzed using a Berkeley Nucleonics 2500R multichannel analyzer, which produces the spectrum of counts or count rate as a function of gamma ray energy. The broad peaks around channels 400, 1180, and 1620 correspond to the main gamma photopeaks from the decay of ^{95m}Tc, with energies of 204, 766, 786, 820, 835, and 1039 keV. To minimize the contribution of background radiation to the spectrum, the detector and sample were mounted inside an enclosure shielded with lead bricks. As shown in the left spectrum in Fig. 5, this reduced the background count rate to a negligible level.

The spectrum on the right shows a restricted range which contains the higher energy photopeaks. The blue reference spectrum was obtained after the activated component was received. The red spectrum was obtained after one erosion experiment. The count rates in that spectrum have been corrected for natural decay over the period of time since the reference spectrum was measured, so the drop in amplitude is due to loss of activated material by erosion. The activity level is proportional to the area under the spectrum, which can be determined by summing the counts within a given energy range. The relative activity between two spectra can also be determined by a least squares analysis of the count rate data.[36]

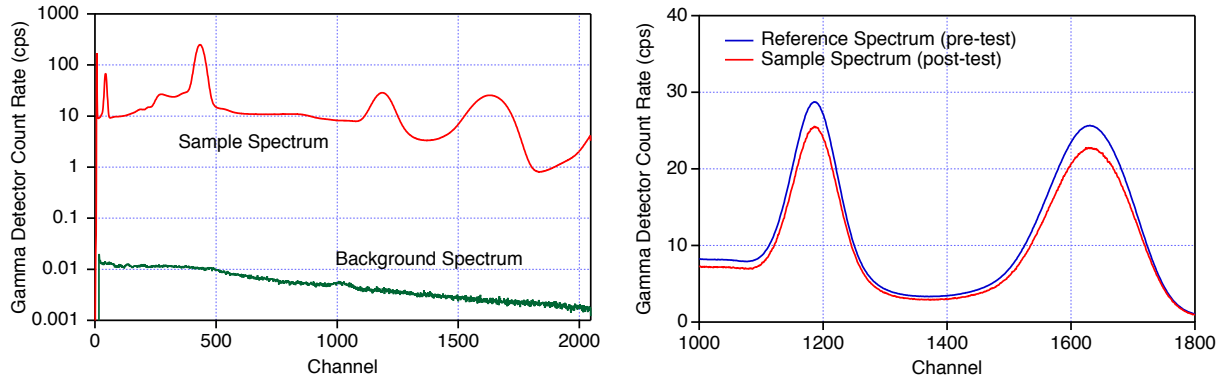

Figure 5. Gamma ray spectra for the activated pole segments.

C. The Depth Calibration Curve

The depth calibration curve is the key to determining the eroded depth based on a measurement of the fraction of the original activity remaining. The curve depends on the distribution of the radioactive tracer as a function of depth in the activated layer, which is determined by the physics of the bombarding particle beam energy loss in the material and the energy-dependent nuclear reaction cross section described above. It is typically determined empirically by activating a stack of thin foils of a given material and then determining the level of activity in each foil or by activating a sample of the bulk material, lapping thin layers off of the surface, and measuring the residual activity as a function of the amount of material removed. The depth obtained by lapping is generally determined by a combination of profilometry and mass loss measurements.

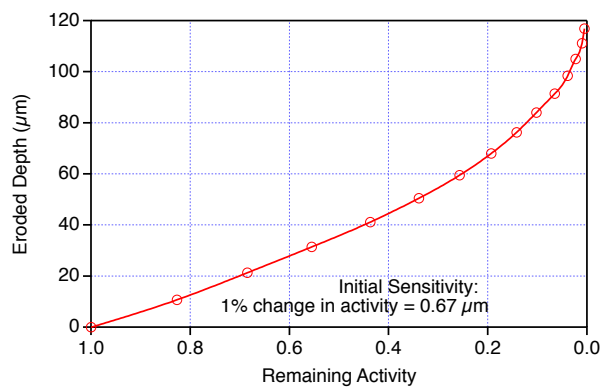

Figure 6. Depth calibration curve for molybdenum activated with an 11 MeV proton beam.

Figure 6 shows the depth calibration curve for molybdenum activated with 11 MeV protons, corrected for compression by a factor of two. The remaining fractional activity or relative activity is the gamma ray count rate in a spectral range of interest measured after removing a certain amount of material, corrected for natural decay, compared to the initial count rate for the entire activated layer. This curve was measured by ANS Technologies using the foil stack method. The first 75% of curve was fit very well with a power law, so this was used for data analysis and in the uncertainty analysis.

III. Erosion Experiments

A. Facility

This experiment was conducted in the Owens Chamber at NASA JPL, which is a 3 m diameter by 10 m long cryogenically pumped vacuum chamber. The facility base pressure was typically 5×10^{-7} Torr and the pressure during testing, measured by a Stabil Ion gauge calibrated on xenon that was mounted next to the thruster, was between 6×10^{-6} and 2.4×10^{-5} Torr.

Ultra-high purity xenon (99.9995% pure) was used as the propellant. The anode and cathode mass flow rates were measured with thermal mass flow meters and the metering valves were mounted in the vacuum chamber so that all external feed lines were above atmospheric pressure to eliminate the possibility of air

leaks into the flow system. All feed system tubing and components have electropolished wetted surfaces and metal seals. The volumetric flow rates were calibrated by measuring the rate of pressure rise in a known volume, yielding flow rate measurements with an uncertainty of less than 2%. A computer data system was used for flow setpoint control and data logging.

Cathode heater, keeper, electromagnet, and discharge power were supplied by computer-controlled commercial power supplies. Mean currents and voltages were measured to within 1% by the data system using calibrated shunts and voltage dividers. A 20 MHz current transformer probe and an 8-bit, 500 MHz Tektronix DPO-3054 digital oscilloscope were used to measure discharge current oscillations during steady-state thruster operation with an accuracy of 2%. The current probe was located on the anode side of the power input between the thruster and discharge filter. Two 25 MHz high-voltage active differential probes were also connected to the oscilloscope to record anode-to-cathode voltage and cathode-to-facility-ground voltage fluctuations with 3% accuracy. Anode and cathode voltage sense lines connected close the thruster ensured the thruster harness-induced voltage characteristics were properly captured in these signals. Oscillations were characterized by calculating the standard deviation (or RMS of the AC coupled signal), peak-to-peak (p-p), and the power spectral density.

Test Order	V_d (V)	V_d^{p-p} (V)	J_d (A)	J_d^{p-p} (A)	J_d freq. (kHz)	Power (kW)	V_k (V)	V_g (V)	Pressure (μTorr)	B-field	Comments
10	300	19.2	10.4	1.6	9.3	3.1	5.2	(V)	6.1	Nom.	
18	300	46.8	15.6	10.5	12.4	4.68	4.09	-14.72	11.0	Nom.	
1	300	28.0	20.8	7.8	13.3	6.2	4.76	-12.63	10.0	Nom.	
12	300	39.2	31.3	9.4	45.1	9.4	6.07	-9.15	19.0	Nom.	
15	400	74.0	15.6	20.2	14.6	6.2	2.66	-14.4	12.0	Nom.	
2	400	63.0	20.8	14.0	11.3	8.3	4.59	-13.1	10.0	Nom.	
16	400	56.0	31.3	9.4	77.1	12.5	5.83	-9.23	20.0	Nom.	
13	500	66.8	12.5	19.6	16.9	6.3	2.14	-13.47	9.8	Nom.	
3	500	90.0	20.8	17.0	51.7	10.4	4.25	-13.05	15.0	Nom.	
14	500	103.0	25	22.2	48.1	12.5	3.64	-10.84	18.0	Nom.	
5	600	74.0	10.3	21.6	16.3	6.2	2.24	-12.74	8.5	Nom.	
6	600	103.0	15.7	16.2	62.1	9.4	0.497	-12.93	11.0	Nom.	
4	600	–	20.8	17.8	–	12.5	4.3	-11.55	13.0	Nom.	
9	600	106.0	20.8	19.0	56.6	12.5	4	-11.56	15.0	Nom.	
17	600	103.0	20.8	18.6	56.4	12.5	4.05	-11.4	16.0	Nom.	
7	600	88.0	20.8	15.8	52.3	12.5	1.64	-10.69	13.0	0.75 x	Off-nom. B
8	600	99.0	20.8	20.0	56.1	12.5	3.99	-13.83	16.0	1.25 x	Off-nom. B
11	600	150.0	20.8	19.0	55.5	12.5	4.39	-11.53	16.0	Nom.	2x Nom. Inductance
19	600	106.0	20.8	21.0	57.5	12.5	4.12	-12.51	24.0	Nom.	P + 8 torr
20	600	107.0	20.8	18.6	56.0	12.5	4.49	-11.61	15.0	Nom.	Cathode Flush with Cover
21	600	26.4	20.8	13.9	57.7	12.5	4.47	-11.6	14.0	Nom.	Very low Inductance

Table 1. Operating Conditions for SLA Erosion Measurements

.

B. Test Conditions

Erosion measurements were made at each of the 21 operating points listed in Table 1. The first 15 points in the table are nominal thruster operating conditions, which are also displayed graphically on the HERMeS thruster throttling envelope in Fig. 7. These points were designed to characterize inner front pole cover erosion at the four throttle curve points (20.8 A discharge current and discharge voltages of 300, 400, 500, and 600 V) and understand how the rates vary with discharge current at a given voltage. The final six test conditions were chosen to study the effect of magnetic field strength, discharge voltage oscillation amplitude (determined by the thruster harness inductance), vacuum chamber pressure, and cathode position. The discharge power supply was operated in constant voltage mode at the setpoints listed in Table 1, the discharge current was controlled at the mean values to within about 0.05 A by varying the anode flow, and the magnetic field configuration was determined by coil current setpoints. The cathode flow fraction was fixed at 7% of the anode flow for all tests. The amplitude and frequency of the current and voltage oscillations and the vacuum chamber pressure listed in Table 1 are the values measured during the tests.

The activity level of each segment was measured after they were activated and before and after each erosion experiment. Custom fixturing ensured that the distance and orientation of the activated spot with respect to the detector was reproduced in each measurement. Multiple spectra were collected at each point with collection times sufficiently long that statistical counting errors were small. Each erosion test lasted between 5.7 and 14 hours, most of which was at the target operating condition. The thruster was always started and operated at low power (10 A and 300 V) to outgas the ceramic discharge chamber. When the current stabilized at fixed flow rate, indicating that most of the water vapor had been outgassed, the current and voltage were ramped up to the final setpoints. In some cases this involved operating briefly at intermediate steps, as shown in Fig. 8. The test campaign was designed to provide erosion rates at most of these intermediate points, and the erosion rates calculated for the final setpoints in a given test were corrected for the erosion that occurred at other conditions during the startup sequence. Erosion rate uncertainties, which averaged about 7% of the measurement value, were calculated from the statistical counting uncertainty, variability due to fixturing, uncertainties in the depth calibration curve, and errors associated with the startup erosion corrections.

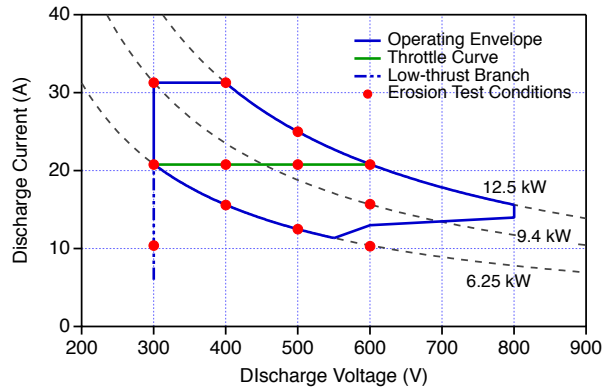

Figure 7. The SLA erosion test points plotted on HERMeS thruster throttling envelope.[6]

C. Cathode Ion Energy Measurements

Some of the surface layer activation test results suggest that high energy ions from the centrally-mounted hollow cathode may be, in part, responsible for pole cover erosion, so a second set of experiments was conducted to characterize this source. It is difficult to instrument the thruster to separate cathode and discharge chamber ions, so a hollow cathode identical to that used in the thruster tests was operated separately with a water-cooled, cylindrical anode. The tests were conducted in a 1.2 m diameter by 3 m long vacuum facility which was pumped by two 25 cm diameter cryopumps. Pressure was monitored with a Granville Phillips Stabil Ion Gauge calibrated with xenon gas. The base pressure was typically 8×10^{-7} Torr and the pressure during cathode operation ranged $1 - 3 \times 10^{-4}$ Torr.

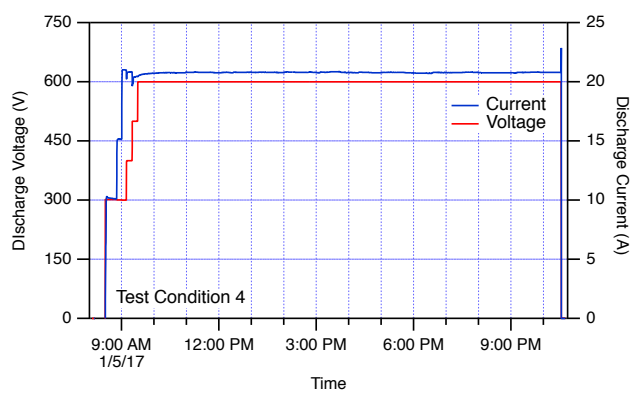

Figure 8. An example of the discharge current and voltage time history for a single erosion measurement showing the startup procedure.

The cathode assembly was mounted inside a solenoid and magnetic circuit similar to the inner coil and circuit components of the thruster. This magnetic circuit reproduced the thruster magnetic field configuration and magnitude in the near-cathode region (a cylinder approximately 4 cm in radius and extending 10 cm downstream of the cathode keeper face).

Ultra-high purity xenon was also used in this experiment and the flow system was similar to the one described above for the thruster erosion experiments. Heater and discharge power were provided by commercial power supplies with the common returns grounded to the vacuum tank. The cathode was also grounded to the chamber through the mounting structure. A separate AC power supply controlled by a function generator was used to superimpose a time-varying current signal on the DC discharge current to simulate current fluctuations experienced by the cathode in the thruster environment. The sinusoidal current oscillations were transformer-coupled into the anode lead. Mean currents and voltages were measured to within 1% by

the data system using calibrated shunts and voltage dividers. The AC current and voltage components were monitored on an oscilloscope using voltage and current probes.

A Hiden EQP energy analyzer and mass spectrometer was used to determine the ion energy distributions of single and double xenon ions. This instrument consists of a 45° sector electrostatic energy analyzer, a triple quadrupole mass filter, and an electron multiplier ion detector with pulse-height analysis electronics for ion counting. The energy analyzer has a range of 0-1000 eV with an energy resolution of 2.55 eV. The mass spectrometer has a range of 1 to 500 AMU and a mass resolution of less than 1 AMU. The detector can detect ion fluxes as low as about 10 counts per second (cps) and as high as 5×10^6 cps. Ideally we would measure the ion energy at the pole cover face, but it's very difficult to access this location. In this experiment the EQP and cathode were configured as shown schematically in Fig. (9). The instrument axis was normal to the cathode axis and intersected it about 5 mm downstream of the cathode keeper face. The 50 micron entrance aperture of the EQP was located about 12 cm from the cathode centerline.

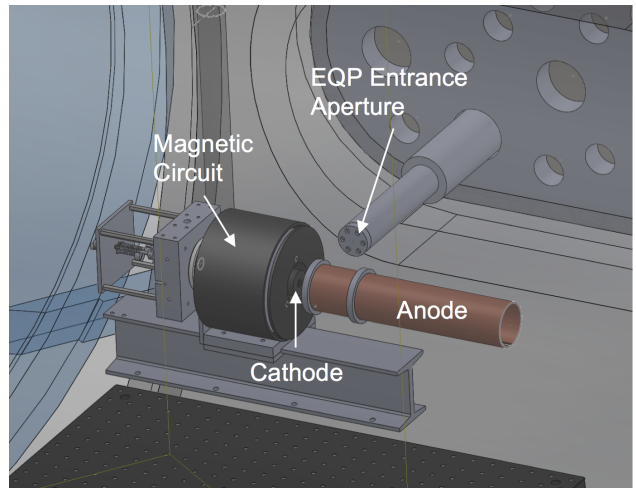

Figure 9. Orientation of the EQP mass and energy analyzer with respect to the hollow cathode.

The acceptance angle of the EQP is less than 2.2° for ions with energies greater than 25 eV, so it samples a conical region with a diameter of about 5 mm at the cathode centerline. This configuration gives an indication of the energies of ions generated in the near-cathode plume which could strike the inner diameter and downstream face of the pole cover, but does not reveal what the corresponding ion fluxes are. Comparisons of the ion signals with and without the magnetic field suggest that the lower energy ion content may be attenuated by the field, perhaps because these ions are deflected out of the instrument field of view by the strong magnetic field in front of the pole piece, so the results may underestimate the lower energy part of the distribution.

The energy distributions of single and double xenon ion generated in the cathode plume were measured for the conditions listed in Table 2. The first four points were designed to reproduce the cathode conditions from the four nominal throttle curve points (20.8 A discharge current at 300, 400, 500, and 600 volts, respectively). The mean current does not include the thruster body current, so it underestimates the total cathode emission current by 1 to 2 A at these conditions. The time-varying current components match the peak-to-peak amplitude and dominant frequency of the oscillations measured during the corresponding SLA measurements. The next three points correspond to conditions at 300 V and a range of discharge currents. The next four points correspond to 600 V thruster operating conditions with varying peak magnetic field strength. The final set of points were designed to explore the effect of current oscillation frequency on the ion energy distributions.

IV. Experimental Results

The erosion rates measured at the five locations on the activated inner front pole cover segments for a discharge current of 20.8 A and voltages ranging from 300 to 600 V (the four nominal points on the throttle curve) are plotted in Fig. 10. The x-axis represents the radial position on the pole cover face normalized by the outer radius r_o minus the inner radius r_i. The values measured on the inner and outer diameters (labelled ID and OD) are shifted slightly from zero and one so they are easier to distinguish from the measurements at the inner and outer positions on the pole cover face. The highest erosion rates occur at 300 V, with strong peaks at the ID, inner face and outer face locations. The erosion rate dips in the center of the pole cover and is also relatively small on the OD surface. At 400–600 V the rates at the ID and inner face locations are similar to those at 300 V, while the rates at the center and outer face locations are lower than the 300 V

J_d (A)	J_d^{p-p} (A)	J_d Freq (kHz)	$\dot{m}_c$ (sccm)	B-field	V_d (V)	V_d^{p-p} (V)	V_k (V)	V_k^{p-p} (V)	$\overline{Y}_C$ (atoms/ion)	$\overline{Y}_{Mo}$ (atoms/ion)	E_{avg} (eV)
10.5	1.58	9.3	7.1	Nom.	25.7	5.2	12.2	1.9	0.0013	0.0068	63
15.5	10.5	12.4	10.1	Nom.	22.2	11.4	8.8	3.5	0.0021	0.0110	72
20.8	7.8	13.3	13.4	Nom.	19.7	7.8	9.4	2.5	0.0013	0.0067	63
31.2	9.4	45.1	18.4	Nom.	16.2	4.9	9.1	4.8	1.7×10^{-6}	3.2×10^{-5}	23
20.8	7.8	13.3	13.4	Nom.	19.7	7.8	9.4	2.5	0.0014	0.0076	64
20.8	14	11.3	13.8	Nom.	19.2	10.3	9.4	3.1	0.0011	0.0060	60
20.8	17	52	14.3	Nom.	18.6	15.2	3.0	14.7	0.00068	0.0036	53
20.8	20	56	14.3	Nom.	18.0	23.3	-0.7	25	0.0006	0.0030	51
10.1	1.58	0	7.1	0	26.1	6	10.9	1.0	0.00058	0.0031	51
10.1	1.58	0	7.1	Nom.	25.3	3.6	12.4	1.7	0.0011	0.0059	60
10.1	1.58	1	7.1	Nom.	25.4	5.4	11.9	2.0	0.00120	0.0065	61
10.1	1.58	5	7.1	Nom.	25.4	5.1	11.9	1.9	0.00120	0.0065	61
10.1	1.58	10	7.1	Nom.	25.4	5.3	11.8	1.8	0.00120	0.0065	61
10.1	1.58	20	7.1	Nom.	25.7	5.9	11.7	1.7	0.00120	0.0064	61
10.1	1.58	30	7.1	Nom.	25.7	6.4	11.5	1.8	0.00120	0.0062	61
10.1	1.58	40	7.1	Nom.	25.7	6.4	11.5	1.9	0.00120	0.0063	61
10.1	1.58	50	7.1	Nom.	25.6	5.9	11.5	2.2	0.00120	0.0062	61
31.2	9.4	0	18.4	0	16.5	0.4	5.6	0.2	2.1×10^{-6}	2.5×10^{-5}	23
31.2	9.4	0	18.4	Nom.	16.1	0.4	10.3	0.3	9.1×10^{-7}	2.6×10^{-5}	22
31.2	9.4	10	18.4	Nom.	15.9	3.2	10.2	1.4	1.1×10^{-6}	2.8×10^{-5}	22
31.2	9.4	45.1	18.4	Nom.	16.2	4.9	9.1	4.8	1.7×10^{-6}	3.2×10^{-5}	23
20.8	20	56	14.5	0	18.4	22.1	-0.8	20.3	0.00010	0.00053	35
20.8	20	56	14.5	0.75 x	17.3	20.1	-0.6	20.5	0.00026	0.0014	42
20.8	20	56	14.5	Nom.	18.1	21.2	-0.5	20.9	0.00056	0.0029	50
20.8	19	56	14.5	1.25 x	18.9	21.4	0.3	21.1	0.00057	0.0030	51

Table 2. Operating Conditions for Cathode Ion Energy Measurements

.

values and suggest that the erosion there is more uniform–they do not exhibit the strong peak in erosion at the outer face observed at 300 V. For the higher voltages no erosion was observed on the OD surface.

In these tests the cathode keeper face was flush with the inner front pole downstream face, so the ID surfaces of the activated pole cover segments were exposed to the cathode plume plasma. The high erosion rates observed on the ID and inner face segments motivated the additional experiments with the cathode simulator to determine whether the cathode could be a source of high energy ions that contribute to wear in these regions. The downstream half of the OD surface protrudes downstream of the ceramic discharge channel sidewall, so only this portion was activated. In most of the experiments the upstream half of the OD surface experienced net deposition of carbon backsputtered from the facility, while the downstream half was generally clean. This indicates that it was subject to some energetic ion bombardment, but the results here indicate that the erosion rates there are negligible except at 300 V. These data provide clear evidence that the 300 V operating point is the worst case and experiences particularly high erosion rates on the outer face.

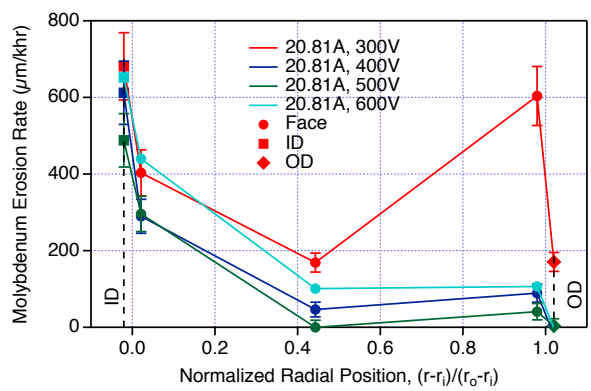

Figure 10. Erosion rates measured on the inner diameter (ID), outer diameter (OD), and downstream face locations for operation at 20.8 A and voltages of 300–600 V.

The effects of discharge current on erosion rates at fixed discharge voltages of 300, 400, 500, and 600 V are displayed in Fig. 11. Five important trends are apparent. The most surprising observation is that the erosion rates at most of the five measurement locations increase monotonically with decreasing current for all four voltage levels–the highest erosion rates occur systematically at the lowest currents. Second, the ID and inner face erosion observed at the lower current levels is mostly or completely suppressed at 31.2 A for

300 and 400 V and decreases significantly for 500 and 600 V. Third, there are two primary erosion sites: the ID surface and adjacent inner face and the outer face. Erosion in the center is lower and, in some cases, undetectable. Fourth, large increases in the erosion rate on the pole cover face occur at 500 V, 12.5 A and at 600 V, 10.4 A cases. Finally, OD edge erosion is negligible for all but the 300 V conditions and 600 V, 10.4 A. In fact, the 600 V, 10.4 A case exhibited higher OD edge erosion than any other experiment, and the entire OD edge surface was cleaned off. This suggests that energetic ions from the discharge channel were much more divergent in that case. However, the ID edge erosion rate did not increase.

The effect of four other parameters was explored in the final set of experiments and the results are summarized in Fig. 12. Increasing the magnetic field strength resulted in higher erosion rates, particularly at the ID edge and inner face, as shown in Fig. 12(a). OD edge erosion was detected at the lowest magnetic field strength, but the erosion measured at the adjacent outer face site is still lower than at the higher field strengths. Fig. 12(b) demonstrates that ID edge erosion can be eliminated by moving the cathode downstream so the keeper face is flush with the cover with no impact on erosion rates in other locations. Apparently the keeper shadows the ID edge from the source of high energy ions. The amplitude of discharge voltage fluctuations associated with the thruster current oscillations was varied by changing the harness inductance, but was found to have negligible impact. Voltage oscillations of 26, 103, and 150 V peak-to-peak around a mean value of 600 V resulted in the same erosion rates, as shown in Fig. 12(c). Note that the lowest inductance case was performed after the cathode position was changed, so there was no ID edge erosion in that case. Finally, the facility pressure was artificially increased from 15 to 27 μTorr. As Fig. 12(d) shows, the elevated pressure had no impact on erosion in the center or outer face, but decreased the erosion rate at the ID edge and inner face by about a factor of two.

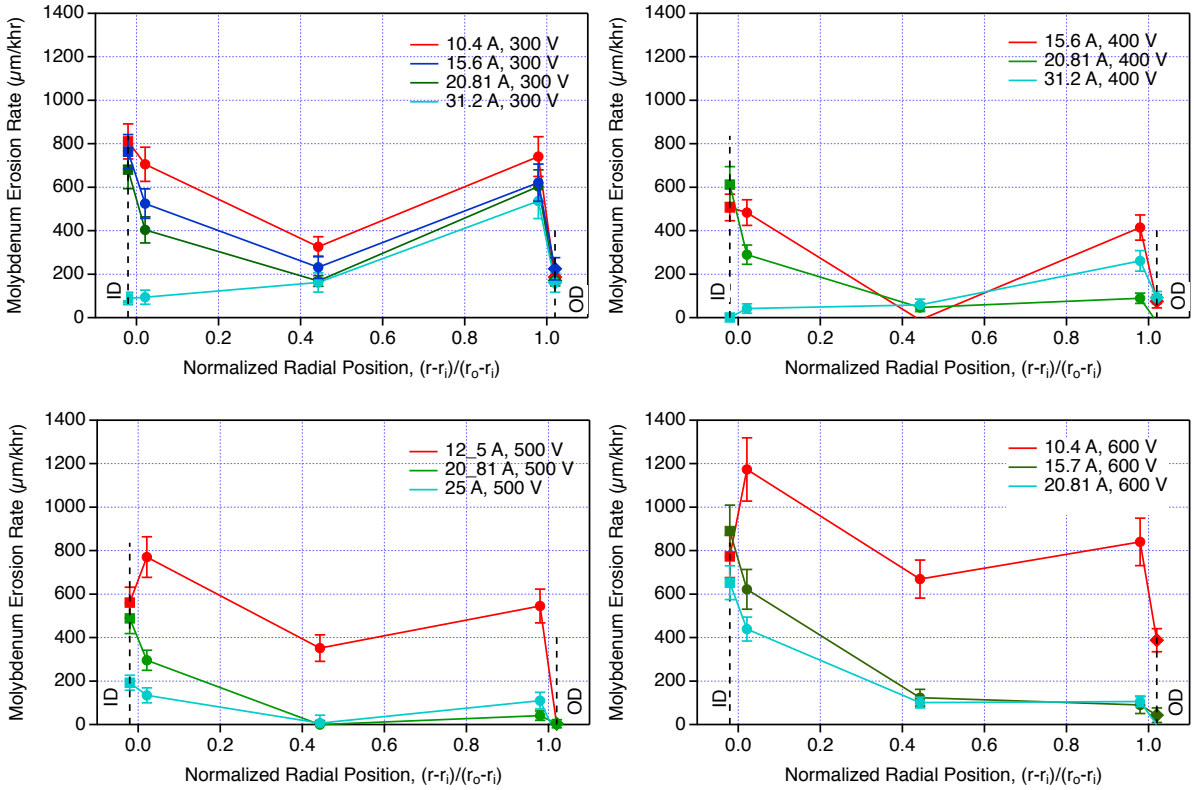

Figure 11. Erosion rates measured at a range of discharge currents for discharge voltages of 300–600 V.

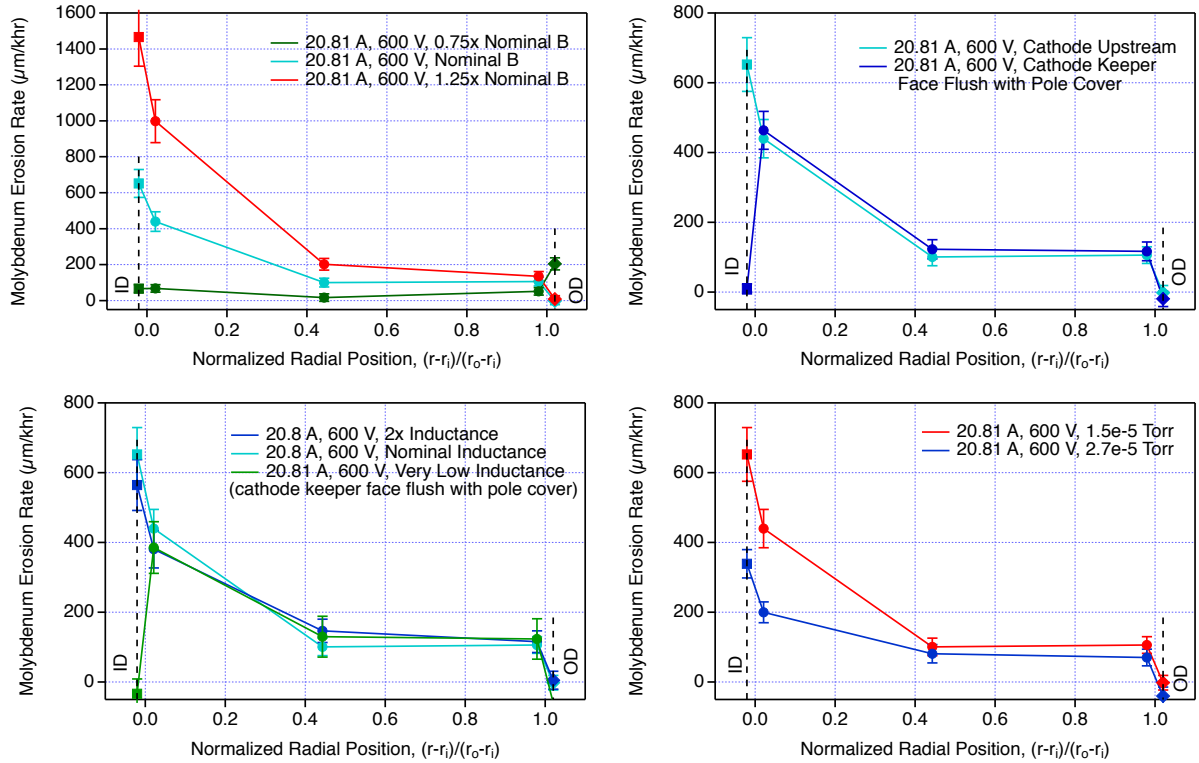

Figure 12. The effect of magnetic field strength, cathode position, discharge voltage oscillation amplitude, and facility pressure on inner pole erosion.

V. Discussion

A. Repeatability of the Erosion Measurements

The uncertainty estimates represented by the error bars in the plots above are based on an assessment of potential error sources, but do they adequately capture variability in the data, due either to intrinsic variability in the fundamental erosion processes or variations in drivers we don't currently understand? To help answer this question, we repeated the 600 V, 20.8 A case several times to test the repeatability of the measurement technique. Some of the other experiments that showed little impact of parameters such as discharge voltage oscillations provided other data sets to compare at this operating point as well. The results of these measurements are summarized in Fig. 13. With the exception of the single measurement labeled "Outlier" in the center location, the repeat measurements agree to within about ± 50–70 μm/khr, which is comparable to the magnitude of the uncertainty estimates. Differences in erosion rates which we observe between various operating parameters that greatly exceed this level are therefore likely to be real effects.

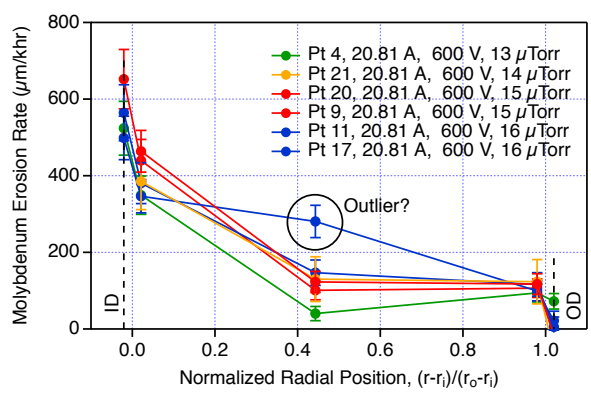

Figure 13. Erosion rates measured at the 600 V, 20.8 A condition. With the exception of one point, the measurements are repeatable to within ±50–70 μm/khr. which is similar to the standard error estimates for a given measurement.

The outlier point in Fig. 13 may be due to measurement error or itan may represent real variability in the

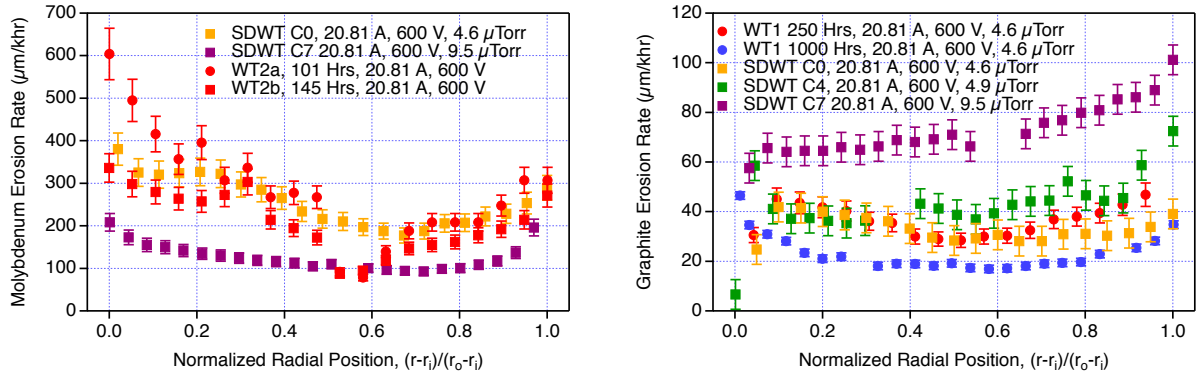

Figure 14. Molybdenum and graphite erosion measurements at the 600 V, 20.8 A condition from the short duration wear tests and the 1722 hour wear test. Variations between measurements of up to a factor of two to three are larger than the uncertainty estimates.

erosion rate at that location. Other points in that particular test agree well with the repeated measurements, and no problems with the gamma spectrum analysis for that point were apparent. Similar behavior was noted by Williams in erosion measurements from the 1722 hour wear test of TDU-1.[21,37] Graphite pole cover and molybdenum witness sample erosion rates obtained by profilometry at 600 V, 20.8 A varied by a factor of two for two different test segments. A subsequent set of short duration wear tests (SDWTs) performed on TDU-1 and TDU-2 for a restricted range of operating parameters exhibited similar variability.[37] Figure 14 summarizes some of these data. Figure 14(a) on the left shows molybdenum erosion rates determined by profilometry on witness samples mounted on the inner front pole cover in the 1722 hour wear test and in the short duration wear tests which vary by a factor of two. Figure 14(b) shows the two sets of graphite pole cover erosion data from the 1722 hour wear test and three sets of data obtained at the same condition in the short duration wear tests. These also vary by a factor of two to three. These effects could also be due to measurement errors, but they are larger than the estimated error bars and no candidate error sources that could explain these large differences have been identified. Williams suggests that operation at elevated pressures could artificially suppress the erosion rate. However, Fig. 14(b) shows a variation of up to a factor of two for multiple data sets taken at a similar pressure and a higher erosion rate for the data obtained at a higher pressure. The molybdenum erosion rates in Figure 14(a) display the opposite trend–erosion rates appear to drop with pressure.

The molybdenum wear rates measured in the short duration wear tests are compared to the surface layer activation erosion measurements in Fig. 15. The results for 300 V agree well at the inner and outer locations while the profilometer measurements are about 50% higher than the SLA measurements in the center region. The profilometer data show the same qualitative shape across the pole cover radius, but are considerably higher than the SLA measurements at 400 and 500 V. Whether these differences are due to facility pressure differences, variability in some other driver, unrecognized experimental errors, or intrinsic variability is not clear. The lower right plot in Fig. 15 shows data from the 600 V test condition obtained at several different facility pressure levels. The SLA results at 27 μTorr agree well with the 9.5 μTorr profilometer data. The 15 μTorr SLA data agree well with the higher pressure profilometer measurements (9.5 μTorr) and the higher pressure SLA data (27 μTorr) at the middle and outer face locations, while the inner face results agree with the low pressure profilometer data (4.6–4.9 μTorr).

The effects of magnetic field strength on the molybdenum erosion rates at 600 V, 20.81 A are compared in Fig. 16. The trend of increasing erosion, particularly at the inner face, is seen in both sets of experiments for molybdenum. However, Williams notes that the corresponding graphite measurements in the short duration wear tests were not as sensitive to magnetic field strength.

B. Contributions to Erosion from Cathode Ions

Several observations suggest that the cathode plume, in addition to the discharge chamber plasma, is a source of high energy ions that contribute to erosion. First, the inner diameter edge is subject to significant

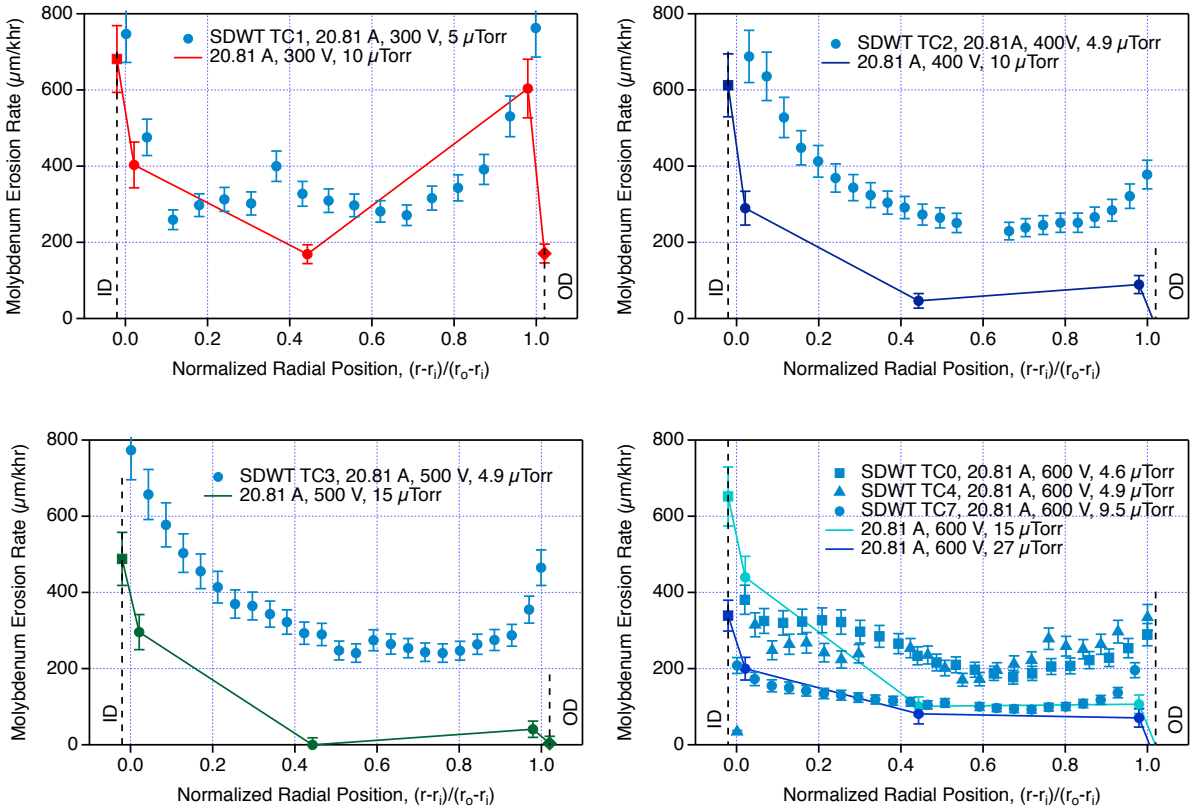

Figure 15. SLA and profilometer erosion rate measurements for similar conditions agree reasonably well at 300 and 600 V, but the SLA erosion measurements are significantly lower at 400 and 500 V.

erosion. Second, the ID edge erosion rates do not change in some cases where large changes are observed in downstream erosion (for example, at 500 V, 12.5 A and 600 V, 10.4 A). In other cases the ID edge and inner face rates change significantly while the middle and outer face rates do not (for example, the 300 and 400 V, 31.2 A cases and the tests in which magnetic field strength and facility pressure were varied). This behavior indicates that there are two populations of energetic ions. The separate cathode experiments confirm that it can be a significant source of energetic ions and revealed trends in the ion energy distributions that match observed trends in erosion rates.

Figure 17 displays the EQP energy and mass analyzer signal for single and double xenon ions as a function of ion energy for the first four points in Table 2. In these experiments the magnetic field configuration and the DC and AC characteristics of the discharge current for the 300 V thruster test conditions were reproduced. The transmission of the instrument is constant over the energy range and the data have been scaled by the natural abundance of the particular isotopes selected for the single and double ions, so the detector count rate is proportional to the ion population in a given energy range. The ion energy distributions are shown on a linear plot on the left, which makes the peak amplitudes easier to compare, and on a semilog plot on the right, which reveals more of the structure of the distributions.

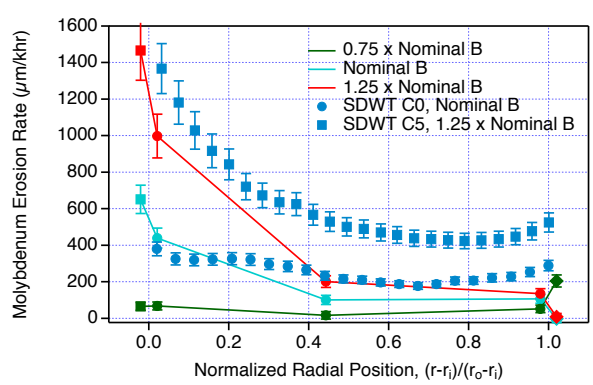

Figure 16. SLA and profilometer erosion measurements show the same trend of increasing rates with increasing magnetic field, particularly at the inner face location.

Three key features are apparent in these data. First, the energies of both single and double ions in the 10.5,

15.5, and 20.8 A cases are high enough to produce high sputter yields. The single ion distributions peak at 40 to 50 eV and the double ion distributions at 85 to 110 eV. We can compare the relative erosion potential of these distributions by calculating the average yield per impacting ion $\overline{Y}$:

$$\overline{Y} = \frac{\int_0^\infty (C_1(E) + C_2(E))Y(E)dE}{\int_0^\infty (C_1(E) + C_2(E))dE} \tag{1}$$

where $C_1(E)$ and $C_2(E)$ are the count rates for single and double ions as a function of energy and $Y(E)$ is the carbon or molybdenum sputter yield as a function of energy. These integrals were calculated from the measured count rates and the Eckstein model for the yields at normal incidence plotted in Fig. 3 using trapezoidal integration. The use of the yields at normal incidence is likely to be conservative in the case of pole cover face erosion because we are sampling ions which would strike the face at glancing angles with higher yields. The average carbon and molybdenum yields and the average ion energy E_{avg} corresponding to those yields are listed in Table 2. For these currents, the sputter yield-weighted average energy of the ions is 63 to 72 eV, which produces non-negligible yields even with graphite. The average energies are higher than the peaks in the single ion populations because the contribution to erosion from double ions is about equal to that from the single ions. These measurements do not give us insight into the fluxes to the pole cover, but these high energies and the fact that the ions are likely to strike the downstream pole cover face with very high incidence angles indicate that this potential source should not be neglected.

Second, in marked contrast, the ion energies for the 31.2 A case are much lower and the double ion fraction is smaller. In this case the average yield is negligible, corresponding to an average energy of only 23 eV. This difference could explain the substantial drop in ID edge and inner face erosion rates observed at 300 and 400 V.

Finally, the ion energies at 10.5, 15.5, and 20.8 A exceed what would be expected for acceleration from the measured anode voltages to ground potential, even considering the anode voltage fluctuations listed in Table 2 which are associated with the current oscillations. The double ion populations appear at twice the energy and show the same structure as the single ion populations, however, which is consistent with an electrostatic acceleration mechanism. We have plans to probe the cathode plume region and may find local potential fluctuations that greatly exceed the discharge voltage, similar to those observed by Goebel.[38] If this is the case, the instabilities which drive these potential oscillations may be damped by higher cathode flow rates or auxiliary gas injection.[39] The ion energy distributions at the 31.2 A condition do peak at energies corresponding to the maximum amplitude of the oscillating discharge voltage, so no additional electrostatic acceleration process is required to explain those distributions.

The second set of cathode tests were conducted with the magnetic field, DC, and AC current characteristics simulating the 20.8 A condition at thruster voltages of 300 – 600 V. The ion energy distributions from these experiments shown in Fig. 18 also peak at high energies, 35 to 40 eV for the singles and 75 to 90 eV for the doubles, and have an even higher proportion of doubly charged ions. In these cases the average

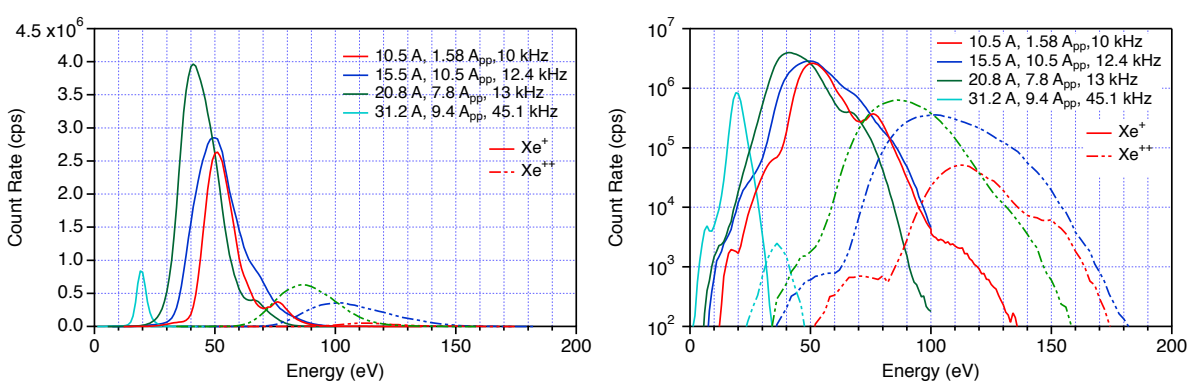

Figure 17. Ion energy distributions measured in cathode experiments simulating thruster operation at 300 V with varying currents.

yields correspond to yield-weighted average energies of 51 to 64 eV, which is high enough to be a credible contributor to the high ID edge and inner front face erosion rates measured at these conditions.

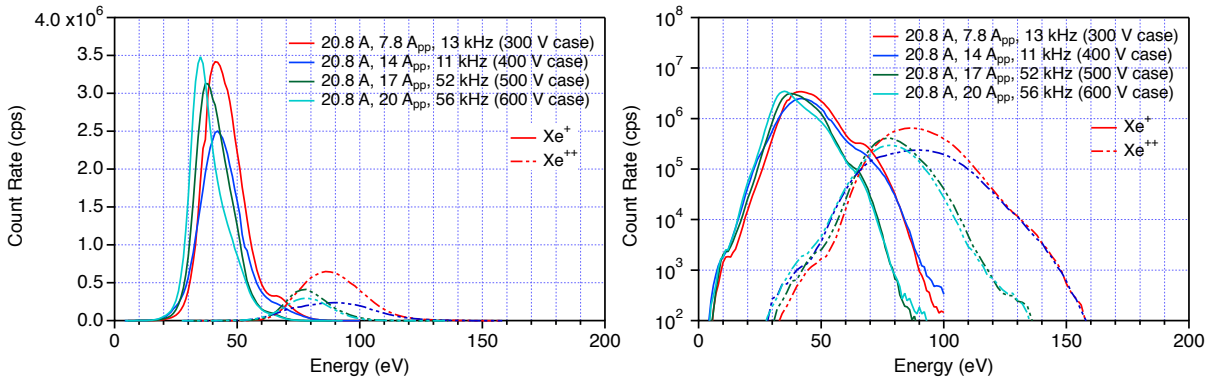

Figure 18. Ion energy distributions measured in cathode experiments simulating thruster operation at 20.8 A with varying voltages.

The 20.8 A cases with lower current oscillation frequencies had slightly higher ion energy content, so we also measured the distributions for 10.1 and 31.2 A over a range of frequencies. Apart from small variations in amplitude of the single and double ion peaks, these distributions were essentially independent of frequency, as the summary data in Table 2 indicate. We did not test the effect of oscillation amplitude, but plan to soon. The ID edge erosion rates for 600 V, 10.4 A and 300 V, 10.1 A are almost identical even though the oscillation amplitudes are dramatically different (21.6 A peak-to-peak vs 1.6 A peak-to-peak). Based on this observation, we predict that ion energy content may not be sensitive to amplitude either.

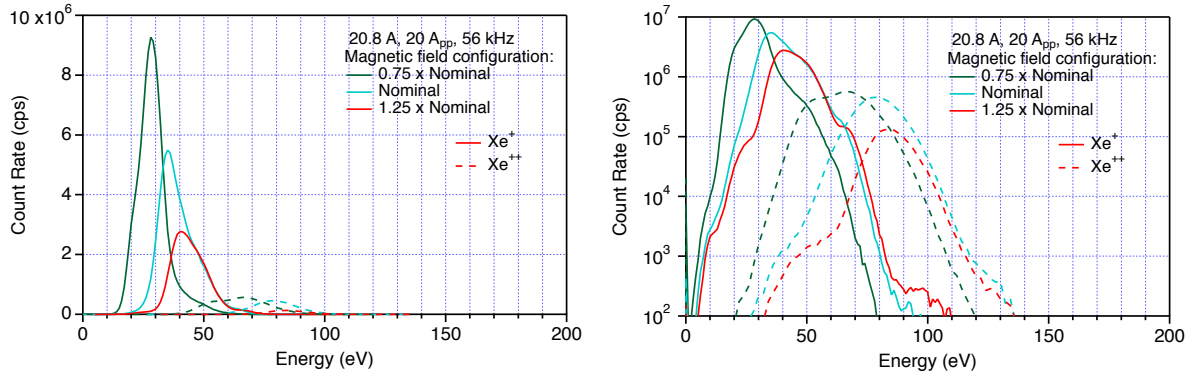

Figure 19. The effect of magnetic field strength on ion energy distributions.

The Hall2De thruster simulation code currently treats cathode plasma as a separate fluid and predicts ion energies much lower than measured here. For the 600 V, 20.8 A condition, the code predicts single, double, and triple ion energies of only 11, 23, and 36 eV. These ions are generated by a mechanism not currently captured in the models which produces a population of ions with characteristics very different from the bulk cathode plasma.

C. Insights from Plasma Simulations and Laser Induced Fluorescence Measurements

The Hall thruster simulation code Hall2De, which was originally developed to study discharge channel erosion, was not initially well-suited for modeling pole erosion. However, a number of advances implemented over the last three years and code benchmarking with laser induced fluorescence (LIF) measurements of the acceleration zone location have made it a much more powerful tool for this application and it provides some insights related to these experimental observations. In turn, the experiments point to processes not currently captured by the models that will require additional work. In this section we review the model updates and

then discuss the ability of the model to capture features noted in the erosion data and how the model results and LIF data illuminate the erosion processes.

Six model improvements, some motivated by the pole erosion problems, have proved to be essential in getting partial agreement with the data obtained to date. In the original code the ions were treated as a single fluid, which yielded accurate results for the beam ions responsible for channel erosion. However, in most cases the beam ions created upstream of the acceleration zone are not responsible for much pole erosion because their trajectories do not intersect the pole face. There are three other populations of ions which do not easily thermalize with the beam ions because of their short residence time, so they are not properly represented by the beam ion fluid. These populations are (1) low energy ions created downstream of the inner pole face between the beam and the cathode plume by charge exchange or cathode plasma electron impact, (2) thruster plume ions born in the acceleration zone or further downstream in the plume which have energies lower than the beam ions, and (3) cathode plume ions. Hall2De has been updated to treat these ion populations as separate fluids or model them as discrete macroparticles using Particle-in-Cell (PIC) methods. LIF measurements of ion velocities near the inner pole and measurements of the plasma potential have shown that the ions created locally near the pole do not have sufficient energy to cause significant sputtering. However, these measurements and modeling showed that the potential distribution at the beam edge creates a pathway for ions generated in the thruster plume to reach the inner pole and they have been identified as a major contributor to erosion in some cases. As noted above, the codes do not currently reproduce the high energy ion populations generated in the cathode plume, which is currently modeled as a separate fluid.

A second improvement is in the way the code treats regions with low plasma density, where the Debye length can approach or exceed the cell size in the mesh. An algorithm which provides an improved potential calculation using the calculated space charge and Poisson's equation led to ion densities between the beam and the cathode that better matched experimental data, potential distributions that allow thruster plume ions to turn toward the pole, and more realistic sheath potentials along the pole face.

Several updates to the code geometry played a role in pole erosion simulations. The details of the geometry between the discharge chamber wall at the channel exit and the outer edge of the inner front pole have an important effect on the local potentials. A higher fidelity boundary model was implemented to better resolve this location. The size of the overall simulation domain was also increased to more accurately capture the interaction between the cathode and thruster plumes. This turned out to impact thruster near-field plume potentials, which control the energy of the ions born in the plume. A related code upgrade was an improved model of anomalous transport in the cathode plume, which was essential to match potential gradients measured downstream of the cathode.

Finally, LIF measurements of ion velocities in the H6MS and TDU-2 thrusters has been instrumental in benchmarking the acceleration zone location for modeling. In the code the location of the potential gradient that accelerates the ions is determined by an empirical model of the anomalous collision frequency. This was informed previously by probe measurements of the potential and electron temperature in the thruster discharge, but these were found to perturb the location of the acceleration zone. An LIF system was then built to make non-intrusive measurements of the ion velocity, from which the potential distribution could be inferred. These data have been used to improve the specification of the anomalous collision frequency profile in the code, reducing a major source of uncertainty in the code results. In addition, the LIF data from these time-averaged measurements and from previous time-resolved LIF measurements suggest that the acceleration zone moves during thruster breathing mode oscillations. This was simulated in the code by specifying a time-dependent spatial profile of the anomalous collision frequency, allowing periodic motion of the acceleration zone with an amplitude and frequency specified by

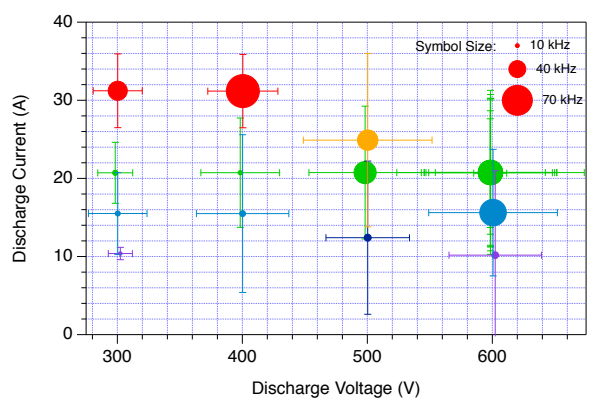

Figure 20. DIscharge current and voltage oscillation amplitude and frequency for the test conditions.

measurements of the discharge current oscillations from thruster tests. This appears to be a primary driver of pole erosion for certain operating conditions.

The characteristics of discharge current and voltage oscillations for the SLA erosion test conditions are summarized in Table 1 and in Fig. 20. The vertical bars in the plot represent the peak-to-peak amplitude of the current oscillations and the horizontal bars are the corresponding peak-to-peak voltage oscillation amplitude. The symbol size is proportional to the frequency of the oscillations, as shown in the legend in the upper right. The symbol colors correspond to particular mean current levels and in some cases the data points have been shifted slightly in voltage to more easily distinguish the vertical bars. The data show that the current oscillation amplitude increases with discharge voltage and is particularly low for the 300 V cases. Two oscillatory modes are apparent–a low frequency mode at lower currents and voltages and a higher frequency mode that occurs as voltage and current are increased.

The Hall2De results for the 600 V, 20.8 A condition agree reasonably well with measured wear rates for graphite. The data are generally higher than the prediction by 50-100%, with the worst agreement at the outer radius of the pole face. The predicted profile drops monotonically with radius, whereas the SLA and profilometer measurements generally show flat or increasing rates at the outer radius. Initial models of wear underpredicted the rates drastically, and the recent success in modeling this condition is primarily due to three of the code improvements discussed above. The addition of the space charge algorithm increased the predicted wear by about a factor of two. The improved boundary geometry between the channel exit and the pole edge increased the predicted wear rate by a factor of about three to five. Finally, including motion of the acceleration zone led to an order of magnitude wear rate increase. These results highlight the importance of the local potential in deflecting plume ions toward the pole and the location of the acceleration zone. Displacement of the acceleration downstream results in higher potentials downstream of the channel exit and gives more high energy ions a line of sight to the pole face. The discrepancy at the outer radius of the pole suggests that further improvements in the local potential model may be required.

The SLA erosion data indicate that the 300 V, 20.8 A condition is the worst case of the nominal throttle points. This finding motivated the subsequent short duration wear tests using TDUs 1 and 3, which confirmed the result. In this case the model underpredicts the erosion rate by a factor of five to ten. The LIF data indicate that the location of the potential profile is not very different at 300 V compared to the mean position at 600 V, but there was no evidence of significant motion. In those tests, as in the SLA tests, the discharge current oscillation amplitude was much smaller than at the 600 V case, so the displacement of the acceleration zone that was crucial to capturing the erosion behavior at 600 V is absent at 300 V. The mechanism for the high erosion rate at 300 V is still not clear. LIF measurements of ion velocities near the beam edge indicate greater beam divergence than predicted by the code. This effect is difficult to reproduce in Hall2De and suggests that code does not currently incorporate the physics required to correctly model the potential gradient along the magnetic field lines. There is either an additional force that is not included or the model of electron transport along the magnetic field is not quite accurate, leading to lower beam divergence. The divergence of the beam ions is not likely to be the cause of the pole erosion at this condition because their trajectories will not intercept the pole. The beam edge potential that causes divergence of the beam ions may also more significantly influence the trajectories of ions generated in the plume which can strike the pole, however.

The SLA results show that the lower current conditions lead to the worst erosion rates overall. Because these points are not on the nominal throttle curve, there has been little simulation work to date. A simulation of a 300 V, 9 A condition yielded erosion rates lower than the 300 V, 20.8 A condition, which already underpredict the wear rates by five to ten times, so the model is unlkely to be able to explain the high wear rates observed in these tests at low voltages. There is currently no LIF data at lower currents to help guide model development. The highest rates overall were observed at 500 V, 12.5 A and 600 V, 10.1 A. As Fig. 20 shows, these conditions had very high discharge current oscillations which were likely associated with large axial displacements of the acceleration zone. This is a likely culprit in these cases, and Hall2De appears to be capable of reproducing erosion driven by this effect well. This should be verified with simulations and LIF measurements.

The SLA tests with varying magnetic field strength showed a clear monotonic increase in erosion rate with magnetic field, particularly at the inner face and ID edge of the pole cover. This effect was confirmed in subsequent short duration wear tests for the molybdenum witness samples, but the graphite data do not

show this trend. As Williams suggests, this may be an artifact of an increased flux of relatively low energy ions at higher magnetic field strengths, for which molybdenum has a higher acceleration factor. Hall2De provides some interesting insights however, which suggest that this may be a significant issue for high voltage operation. LIF data obtained at 300 - 600 V with these three magnetic field values show that in most cases the acceleration zone moves upstream as the field strength increases. This would generally be expected to reduce the erosion rate, and in fact the code results show this for the lower voltage cases. However, at 600 V the code predicts increased erosion similar to that observed in the tests. In this case the motion of the acceleration zone associated with high amplitude current oscillations mitigates the upstream displacement to some extent. In addition, the code predicts that the higher magnetic field strength on centerline increases the resistance in the cathode plume, resulting in higher plasma potential in the near-field thruster plume. There are no probe measurements of potential in the HERMeS thruster to verify this, but the results are consistent with plume potentials inferred from the LIF ion velocity measurements. The increased near-field plume potential affects the energy of ions born in the plume which can reach the poles, so this is an unexpected driver of erosion. The HERMeS thruster was designed to operate at much higher magnetic field strengths if necessary, but this effect needs to be understood to determine if this additional magnetic field margin could actually be used without sacrificing pole cover life.

VI. Conclusions

The use of molybdenum pole covers to accelerate the wear rates and the highly sensitive surface layer activation technique enabled rapid testing over a wide range of conditions yielding data which otherwise the program would not have been able to afford to collect in longer duration wear tests. The results allowed us to identify the worst case condition amongst the nominal throttle points, identified the main drivers for pole erosion, and provided more guidance and validation data for the modeling effort.

These test provided the first data to show that the 300 V, 20.8 A condition is the worst case. This was confirmed in subsequent short duration wear tests for molybdenum and graphite. Higher voltage operation at 20.8 A produced lower rates that did not vary as much with voltage This result cannot currently be reproduced by the Hall2De code, which yields rates that are about an order of magnitude too low. LIF data suggest that the beam ions are more divergent in this case than the model predicts, and this may be the key piece of physics that is missing. More work is required to understand the mechanism in this case, which is particularly critical because it is a point on the main throttle curve.

The measurements also produced the first data showing that the lowest current levels produced the highest erosion rates. The 31.2 A case at 300 and 400 V appears to be relatively benign. This behavior at low voltage is also not currently reproduced by simulations conducted for operation at 300 V, 9 A. The predicted rates are lower than those measured or calculated for 300 V, 20.8 A. LIF measurements at the low current conditions may provide additional clues to help identify the mechanisms of erosion at low voltages.

The physics in Hall2De have been significantly improved over the last three years and it is now much more capable of reproducing the erosion observed at 600 V, 20.8 A. A primary driver in this case is the motion of the acceleration zone associated with breathing mode oscillations. This is likely the explanation for the high erosion rates observed for low current levels at 500 and 600 V, which were also subject to high amplitude current fluctuations. This conclusion should be verified with simulations and LIF measurements at these lower current levels.

The SLA measurements at a number of operating points indicated high erosion rates at the inner face and the inner diameter edge of the pole cover, which suggested that the cathode could be an additional source of high energy ions. To test for this, a separate cathode experiment was performed and high energy ions were indeed observed at the conditions with high wear rates at these locations. The Hall2De code does not currently predict these high energy ions. Additional testing is planned to further characterize the cathode ion energy content, and if they confirm the preliminary findings, the mechanism should be identified and incorporated in the simulations.

VII. Acknowledgments

The support of the joint NASA GRC and JPL development of HERMeS by NASA's Space Technology Mission Directorate through the Solar Electric Propulsion Technology Demonstration Mission project is gratefully acknowledged. The authors would also like to acknowledge the assistance of Yves Trudeau at ANS Technologies in planning for and activating the parts used in these experiments. The research described in this paper was carried out at the Jet Propulsion Laboratory, California Institute of Technology, under a contract with the National Aeronautics and Space Administration.

References

[1]Herman, D., Tofil, T., Santiago, W., Kamhawi, H., Polk, J., Snyder, J., Hofer, R., Picha, F., Jackson, J., and Allen, M., "Overview of the Development and Mission Application of the Advanced Electric Propulsion System (AEPS)," 35th *International Electric Propulsion Conference*, Atlanta, Ga., 2017, IEPC 2017-284.

[2]Manzella, D. and Hack, K., "High-Power Solar Electric Propulsion for Future NASA Missions," *50th Joint Propulsion Conference*, Cleveland, OH, 2014, AIAA-2014-3718.

[3]Mcguire, M., Hack, K., Manzella, D., and Herman, D., "Concept Designs for NASA's Solar Electric Propulsion Technology Demonstration Mission," *50th Joint Propulsion Conference*, Cleveland, OH, 2014, AIAA-2014-3717.

[4]Brophy, J. and Randolph, T., "Status of the Asteroid Redirect Robotic Mission (ARRM)," 35th *International Electric Propulsion Conference*, Atlanta, Ga., 2017, IEPC 2017-031.

[5]Gerstenmaier, W., "Progress in Defining the Deep Space Gateway and Transport Plan," *Meeting of the HEO Committee of the NASA Advisory Council*, NASA Headquarters, 2017, `https://www.nasa.gov/sites/default/files/atoms/files/nss_chart_v23_tagged.pdf`.

[6]Hofer, R., Polk, J., Mikellides, I., Ortega, A. L., Conversano, R., Chaplin, V., Lobbia, R., Goebel, D., Kamhawi, H., Verhey, T., Williams, G., Mackey, J., Huang, W., Yim, J., et al., "Development Status of the 12.5 kW Hall Effect Rocket with Magnetic Shielding (HERMeS)," 35th *International Electric Propulsion Conference*, Atlanta, Ga., 2017, IEPC 2017-231.

[7]Kamhawi, H., Huang, W., Haag, T., Yim, J., Herman, D., Peterson, P., Williams, G., Gilland, J., Hofer, R., and Mikellides, I., "Performance, Facility Pressure Effects, and Stability Characterization Tests of NASA?s Hall Effect Rocket with Magnetic Shielding Thruster," *52nd Joint Propulsion Conference*, Salt Lake City, UT, 2016, AIAA-2016-4826.

[8]Jackson, J., Allen, M., Myers, R., Soendker, E., Welander, B., Tolentino, A., Hablitzel, S., Yeatts, C., Sheehan, C., Cardin, J., Tofil, T., Herman, D., Snyder, J., and Hofer, R., "13 kW Advanced Electric Propulsion Flight System Development and Qualification," 35th *International Electric Propulsion Conference*, Atlanta, GA, 2017, IEPC 2017-223.

[9]Grys, K. D., Mathers, A., Welander, B., and Khayms, V., "Demonstration of 10,400 Hours of Operation on 4.5 kW Qualification Model Hall Thruster," *46th Joint Propulsion Conference*, Nashville, TN, 2010, AIAA-2010-6698.

[10]Mikellides, I., Katz, I., Hofer, R., Goebel, D., de Grys, K., and Mathers, A., "Magnetic Shielding of the Channel Walls in a Hall Plasma Accelerator," *Physics of Plasmas*, Vol. 18, No. 3, 2011, pp. 033501, doi: 10.1063/1.3551583.

[11]Mikellides, I. and Katz, I., "Numerical Simulations of Hall-effect Plasma Accelerators on a Magnetic-Field-Aligned Mesh," *Physical Review E*, Vol. 86, 2012, pp. 046703, doi: 10.1103/PhysRevE.86.046703.

[12]Mikellides, G., Katz, I., Hofer, R., and Goebel, D., "Magnetic Shielding of a Laboratory Hall Thruster Part I: Theory and Validation," *J. Appl. Phys.*, Vol. 115, 2014, pp. 043303.

[13]Hofer, R., Goebel, D., Mikellides, G., and Katz, I., "Magnetic Shielding of a Laboratory Hall Thruster Part II: Experiments," *J. Appl. Phys.*, Vol. 115, 2014, pp. 043303.

[14]Hofer, R., Jorns, B., Polk, J., Mikellides, I., and Snyder, J., "Wear Test of a Magnetically Shielded Hall Thruster at 3000 Seconds Specific Impulse," 33rd *International Electric Propulsion Conference*, Washington, DC, 2013, IEPC 2013-033.

[15]Mikellides, G., Katz, I., Hofer, R., and Goebel, D., "Magnetic Shielding of Hall Thrusters at High Discharge Voltages," *J. Appl. Phys.*, Vol. 116, 2014, pp. 053302.

[16]Kamhawi, H., Huang, W., Haag, T., Shastry, R., Soulas, G., Smith, T., Mikellides, I., and Hofer, R., "Performance and Thermal Characterization of the NASA-300ms 20 kW Hall Effect Thruster," 33rd *International Electric Propulsion Conference*, Washington, DC, 2013, IEPC 2013-444.

[17]Shastry, R., Huang, W., and Kamhawi, H., "Near-Surface Plasma Characterization of the 12.5-kW NASA TDU1 Hall Thruster," *51st Joint Propulsion Conference*, Orlando, FL, 2015, AIAA-2015-3919.

[18]Ortega, A. L., Mikellides, I., and Chaplin, V., "Numerical Simulations for the Assessment of Erosion in the 12.5-kW Hall Effect Rocket with Magnetic Shielding (HERMeS)," 35th *International Electric Propulsion Conference*, Atlanta, GA, 2017, IEPC 2017-154.

[19]Mikellides, I. and Ortega, A. L., "Assessment of Pole Erosion in a Magnetically Shielded Hall Thruster Ioannis," *50th Joint Propulsion Conference*, Cleveland, OH, 2014, AIAA-2014-3897.

[20]Sekerak, M., Hofer, R., Polk, J., Jorns, B., and Mikellides, I., "Wear Testing of a Magnetically Shielded Hall Thruster at 2000 s Specific Impulse," 34th *International Electric Propulsion Conference*, Hyogo-Kobe, Japan, 2015, IEPC 2015-155.

[21]Williams, G., Gilland, J., Peterson, P., Kamhawi, H., Huang, W., Ahern, D., Yim, J., Herman, D., and Hofer, R., "Wear-Testing of the 12.5 kW HERMeS Technology Demonstration Unit One," 63rd *JANNAF Propulsion Meeting*, 2016.

[22]"The Thin Layer Activation Method and its Application in Industry," Tech. Rep. IAEA-TECDOC-924, ISSN 1011-4289, International Atomic Energy Agency, 1997.

[23]Kolasinski, R. and Polk, J., "Characterization of Cathode Keeper Wear by Surface Layer Activation," *J. Prop. and Power*, Vol. 20, No. 6, 2004, pp. 992–999, doi.org/10.2514/1.6191.

[24]Kolasinski, R. and Polk, J., "Cathode Keeper Orifice Wear Measurements Using Surface Layer Activation," 41st *Joint Propulsion Conference*, Tucson, AZ, 2005, AIAA-2005-3664.

[25]Yim, J., "A Survey of Xenon Ion Sputter Yield Data and Fits Relevant to Electric Propulsion Spacecraft Integration ," 35th *International Electric Propulsion Conference*, Atlanta, Ga., 2017, IEPC 2017-060.

[26]Conlon, T. W., "Thin Layer Activation," *Tribology International*, 1979, pp. 60–64.

[27]Conlon, T. W., "Doping Surfaces with Radioactive Atoms–for Research and Industry," *Contemp. Phys.*, Vol. 23, No. 4, 1982, pp. 353–369.

[28]Conlon, T. W., "Ion Beam Activation for Materials Analysis: Methods and Applications," *IEEE Trans. Nucl. Sci.*, Vol. 28, No. 2, 1981, pp. 1816–1819.

[29]Conlon, T. W., "Nuclear physics for materials technology: Accelerator based methods," *Contemp. Phys.*, Vol. 26, No. 6, 1985, pp. 521–558.

[30]Blatchley, C. and Sioshansi, P., "Surface Layer Activation Technique for Monitoring and In Situ Wear Measurement of Turbine Components," *Jet Propulsion*, Vol. 3, No. 3, 1986, pp. 248–252.

[31]Asher, J., Conlon, T., Tofield, B., Sugden, S., and Lawrence, P., "Experience of Plant Corrosion Monitoring By Thin Layer Activation," *Corrosion '86*, Houston, TX, March 17-21,1986, Paper Number 131.

[32]Read, P., Asher, J., Conlon, T., and Sofield, C., "Unipolar Arc Erosion Rates Measured Using an Ion Beam Activation Technique," *Journal of Nuclear Materials*, Vol. 99, 1981, pp. 235–242.

[33]Polk, J., Kelly, A. J., and Jahn, R. G., "Measurement of MPD Thruster Erosion Using Surface Layer Activation," *AIAA Journal of Power and Propulsion*, Vol. 3, No. 1, 1987, pp. 33–38.

[34]Polk, J., Kelly, A. J., and Jahn, R. G., "Characterization of Cold Cathode Erosion Processes," 20th *International Electric Propulsion Conference*, Garmisch-Partenkirchen, W. Germany, 1988, AIAA-88-075.

[35]Polk, J., Kelly, A., and Jahn, R., "Mechanisms of Hot Cathode Erosion in MPD Thrusters," 21st *International Electric Propulsion Conference*, Orlando, FL, 1990, AIAA-90-2673.

[36]Schonfeld, E. et al., "Determination of Nuclide Concentrations in Solutions Containing Low Levels of Radioactivity by Least-Squares Resolution of the Gamma-Ray Spectra." *Nuclear Instruments and Methods*, Vol. 45, 1966, pp. 1–21.

[37]Williams, G., Kamhawi, H., Choi, M., Haag, T., Huang, W., Herman, D., Gilland, J., and Peterson, P., "Wear Trends of the HERMeS Thruster as a Function of Throttle Point," 35th *International Electric Propulsion Conference*, Atlanta, Ga., 2017, IEPC 2017-207.

[38]Goebel, D., Jameson, T., Katz, I., and Mikellides, I., "Energetic Ion Production and Keeper Erosion in Hollow Cathode Discharges ," 29th *International Electric Propulsion Conference*, Princeton, NJ., 2005, IEPC-2005-266.

[39]Chu, E. and Goebel, D., "High-Current Lanthanum Hexaboride Hollow Cathode for 10-to-50 kW Hall Thrusters," *IEEE Trans. Plasma Sci.*, Vol. 40, No. 9, 2012, pp. 2133–2144.